Research Article Vol. 34, No. 5 / 9 Mar 2026 / Optics Express 7496
Optics EXPRESS

Single-frame randomized probe imaging in the EUV using a high-order harmonic source

Soo Hoon Chew,[1,2,*] Wilhelm Eschen,[1,3,4] Chang Liu,[1,3,4] Mahmoud Abdelaal,[1] Jens Limpert,[1,2,3,4] and Jan Rothhardt[1,2,3,4]

[1]Institute of Applied Physics and Abbe Center of Photonics, Friedrich Schiller University Jena, Albert-Einstein-Straße 15, 07745 Jena, Germany
[2]Fraunhofer Institute for Applied Optics and Precision Engineering, Albert-Einstein-Straße 7, 07745 Jena, Germany
[3]Helmholtz Institute Jena, Fröbelstieg 3, 07743 Jena, Germany
[4]GSI Helmholtzzentrum für Schwerionenforschung, Planckstraße 1, 64291 Darmstadt, Germany
[*]soohoon.chew@uni-jena.de

Abstract: We report the demonstration of single-frame randomized probe imaging (RPI) using a 13.5 nm extreme ultraviolet (EUV) beam from a table-top high-harmonic generation (HHG) source. Three types of beams—a smooth, vortex, and speckle beam—were used to investigate the effect of different illuminations on image quality. Single-frame RPI reconstructions were successfully achieved for all beam types, with the highest resolution of 110 nm obtained using the EUV speckle beam. Comparisons with ptychography reconstructions confirm the advantages of structured illuminations over a smooth beam, showing improved convergence and image fidelity. Furthermore, averaging a small number of RPI images reconstructed from individual diffraction patterns significantly improves the resolution to sub-100 nm. These results demonstrate the capability of single-frame RPI to deliver rapid, high-resolution EUV imaging, offering a promising approach for applications limited by acquisition time, such as ultrafast pump-probe studies and real-time feedback.

1. Introduction

Imaging in the extreme ultraviolet (EUV) and soft X-ray regimes offers a wide range of advantages. Their short wavelengths allow for high-resolution imaging on the nanometer scale [1–3]. Moreover, nearly every element exhibits absorption edges in this spectral range, making it ideal for acquiring material-specific information about samples [4]. This spectral range also provides access to several transmission windows [5], enabling the investigation of micrometer-thick samples. In practice, however, the resolution achievable in conventional EUV and X-ray microscopes is not limited by the wavelength, but rather by the technological feasibility of the optics.

To overcome this limitation, modern computational imaging techniques have been developed and applied from the visible down to the X-ray region in the past decades [3,6,7]. Collectively known as lensless imaging modalities, these approaches eliminate the need for imaging lenses altogether. Instead, a coherently illuminated object produces a diffraction pattern, which is then computationally reconstructed using phase retrieval algorithms to recover the image [8,9]. So far, lensless imaging experiments have primarily been conducted at synchrotrons [10,11] and free-electron lasers [10,12–14] due to their high brilliance, which has enabled groundbreaking discoveries in fields such as nanotechnology [15–17], biology [17–19], and materials science [17,20].

#580785 https://doi.org/10.1364/OE.580785
Journal © 2026 Received 2 Oct 2025; revised 20 Dec 2025; accepted 22 Dec 2025; published 24 Feb 2026

Optics EXPRESS

Recently, however, femtosecond lasers have undergone rapid development, enabling compact, coherent EUV and soft X-ray sources based on high-harmonic generation (HHG) [21]. These sources can cover a spectral range extending into the X-ray region [22–26] and offer brightness in the long-wavelength EUV range [27,28] that was previously available only at state-of-the-art synchrotron facilities. Combining such coherent sources with modern lensless imaging techniques now allows for laboratory-scale imaging experiments that were previously exclusive to synchrotron facilities [29,30]. Furthermore, HHG inherently produces ultrafast pulse trains with durations down to the attosecond range [31,32]. This enables not only high spatial resolution but also exceptionally high temporal resolution [33], which has been extensively exploited in pump-probe spectroscopy to gain unique insights into electron dynamics of atoms [31,34–36], molecules [37–39], and solids [40–44]. The combination of ultrafast HHG sources with modern lensless imaging modalities thus promises simultaneous nanoscale spatial resolution and temporal resolution in the femto- to attosecond range [45].

In recent years, three methods have become prominent for lensless imaging using HHG sources: classical coherent diffractive imaging (CDI) [8,9,46,47], mask-based Fourier transform holography (FTH) [48–50], and ptychography [51–53]. Both CDI and FTH are limited to isolated samples and require sophisticated sample preparation. In contrast, ptychography allows for the investigation of arbitrarily extended samples. However, ptychography is a scanning microscopy technique that poses challenges for pump-probe measurements. The requirement to scan both the illumination across the sample and the time delay considerably increases the overall acquisition time. Therefore, a methodology for ultrafast imaging experiments is desirable, one that enables arbitrary samples to be captured in a single frame without scanning. A promising approach in this context is randomized probe imaging (RPI) [54], which is a form of coherent modulation imaging [55,56]. Briefly, in RPI, the illumination function is first characterized using ptychography. The object is then reconstructed from a single diffraction pattern using an iterative phase retrieval algorithm that incorporates the pre-characterized illumination function and a band-limited constraint.

In this work, we demonstrate single-frame RPI for the first time using a table-top HHG source at 13.5 nm wavelength. We investigate the influence of illumination shape and angular spectrum on image quality in RPI. Our findings indicate that highly structured illumination significantly enhances the image quality. Under optimized illumination conditions, we achieve a spatial resolution down to 110 nm from a single diffraction pattern. Averaging multiple images further leads to substantial improvements in resolution and overall image clarity. Importantly, RPI is highly robust and enables quantitative object transmission function reconstruction rather than merely retrieving the exit surface wave. It also features a straightforward experimental geometry, requires no reference hole, and is, like ptychography, applicable to arbitrary samples without an isolation constraint, and potentially to reflection imaging. This advancement paves the way for high-resolution, ultrafast pump-probe studies of solid-state samples, as well as real-time image reconstructions in ptychography experiments.

2. Methodology

Figure 1 (a) depicts the experimental setup used for both EUV ptychography and single-frame RPI in this work. The spatially coherent HHG source used for the imaging is driven by a few-cycle femtosecond laser (<10 fs) with a central wavelength of 1030 nm and a pulse energy of 0.4 mJ, provided by a Yb-doped fiber laser system combined with two nonlinear compression stages. This source features a broadband EUV continuum extending up to 100 eV and achieves a photon flux of 7×10^9 $(\mathrm{s} \cdot \mathrm{eV})^{-1}$ at 13.5 nm (92 eV) [57]. It exhibits excellent power stability of better than 1% root mean square (rms) and beam pointing stability of 1 µrad rms over the duration of the experiments, indicating high probe beam stability, which is crucial for the performed imaging measurements. The HHG-EUV beam illuminating the target sample has a central

Optics EXPRESS

wavelength of 13.5 nm with a bandwidth of 0.23 nm after selective spectral filtering. The sample consists of milled-through structures patterned by a focused beam on a 500 nm thick silicon film, which is coated on a 50 nm thick Si_3N_4 membrane. A mask is positioned approximately 200 µm before the sample to tailor the illuminating beam. One of three masks with an aperture of about 8 µm can be selected for each imaging experiment, resulting in three different illuminations: an unstructured beam produced by a pinhole, a vortex-shaped structured beam generated by a binary spiral amplitude mask [58], and a highly randomized speckle pattern created by a phase-shifting EUV diffuser mask [59]. The diffraction patterns from the sample are recorded by a scientific complementary metal-oxide-semiconductor (sCMOS) detector with a resolution of 2048 × 2048 pixels and a pixel size of 11 µm × 11 µm placed 30 mm behind the sample [60]. All diffraction pattern images were cropped to 1024 × 1024 pixels, while the maximum dynamic range images in Fig. 3 were cropped to 1536 × 1536 pixels prior to reconstruction, as the patterns occupy only the central region of the images.

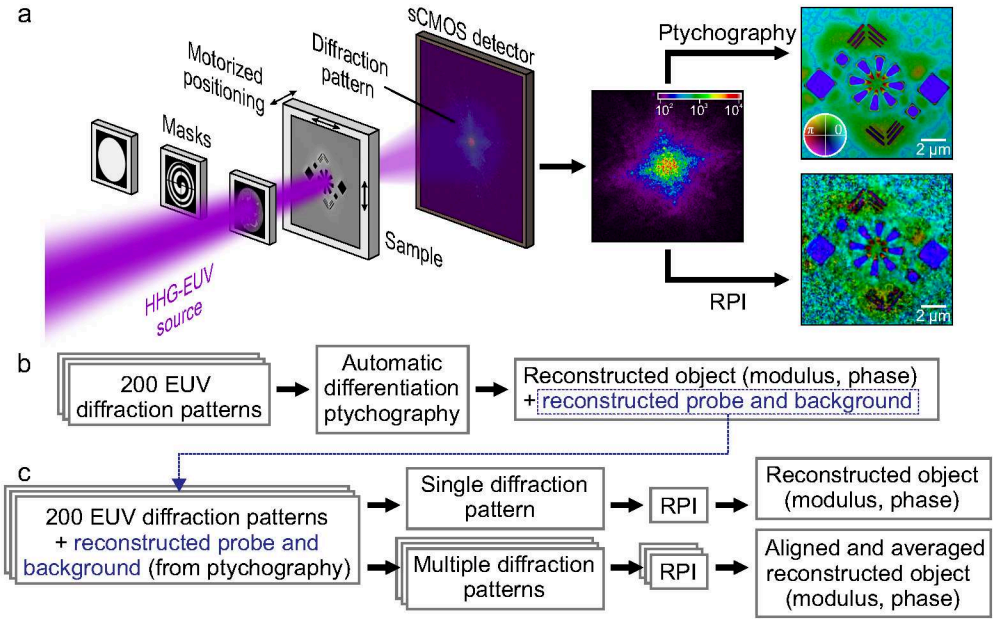

Fig. 1. (a) Schematic setup of EUV ptychography and single-frame RPI. An HHG-EUV beam is directed through a mask onto a sample. One of three masks (from left to right: pinhole, spiral, or diffuser) can be selected for each imaging. The diffraction patterns formed after the sample are recorded by an sCMOS detector and subsequently processed using ptychography and RPI algorithms, respectively. A representative far-field diffraction pattern using the diffuser mask is shown on a logarithmic scale. Exemplary images reconstructed by both algorithms using the diffuser mask are shown, as they yield the highest image quality. Color wheel: phase is represented as hue and modulus as brightness. (b) Workflow for EUV ptychography reconstruction. (c) Workflow for EUV single-frame RPI reconstruction.

Each EUV ptychography measurement was performed by scanning the sample in a spiral pattern with a step size of 1 µm across 200 positions using a motorized positioner, resulting in 200 diffraction patterns. The ptychographic datasets [59] were then reconstructed with an automatic differentiation-based ptychography algorithm [61,62], employing a mixed-state model [63] with four probe modes. The reconstructions were performed on a workstation with a graphics processing unit (Nvidia RTX A6000) and took about 20–30 min each depending on the image resolution. As a result, the complex transmission function of the object (sample) in terms of

Optics EXPRESS

modulus and phase, as well as the probe (illuminating beam) and a constant background (e.g., due to stray light or dark current), can be retrieved (Fig. 1 (b)). These probe and background data obtained from ptychography were then provided to an RPI algorithm [54], which can reconstruct the modulus and phase image from a single diffraction pattern selected from the scan (Fig. 1 (c)). In essence, the RPI algorithm operates by imposing a band-limited constraint on the object within the automatic differentiation-based ptychography framework using the forward model, enabling a unique solution to the phase retrieval problem even with just a single diffraction pattern. Firstly, the randomized probe, also known as the band-limited random illumination, introduces high-frequency phase structures on the wavefield $P(x,y)$. Secondly, a band-limiting constraint is applied to the object transmission function $O(x,y)$ during reconstruction. Specifically, $O(x,y)$ is restricted to a maximum spatial frequency k_0 that is significantly lower than the highest frequency contained in the probe, k_p. As a consequence, when $k_0 \ll k_p$, the diffraction pattern occupies a substantially larger region of Fourier space than the object itself. This ensures that the final diffraction pattern can easily contain more spatial modes than the independent degrees of freedom in a band-limited object, analogous to oversampling, thereby leading to a well-posed inverse problem in the space of band-limited objects. Together, these explicit constraints provide sufficient information to uniquely solve the phase retrieval problem from a single diffraction pattern, without requiring a finite support or multiple diffraction patterns. In short, the forward model up-samples the low-resolution unknown object (via zero-padding in Fourier space), multiplies it by the known high-resolution probe, Fourier transforms the resulting exit wave, and propagates it to the detector. Reconstruction begins with an initial guess of the object, and the error between the measured and the simulated diffraction patterns is calculated. The Wirtinger derivative of this diffraction loss with respect to the object is then used to update the object via the Adam optimization algorithm [64] in order to minimize the loss, and the process is repeated iteratively until convergence. Further details of the RPI reconstruction method can be found in Ref. [54].

The RPI reconstruction was applied to each individual diffraction pattern within the ptychography scan, resulting in 200 individually reconstructed object images differing by the position of the illumination source on the sample (see Visualization 1, Visualization 2, and Visualization 3 for the pinhole, spiral, and EUV diffuser masks, respectively). A single RPI reconstruction typically took about 0.5–1 min on the same workstation. Moreover, we can average the RPI-reconstructed images from multiple individual diffraction patterns to improve the signal-to-noise ratio (SNR) relative to a single reconstruction (Fig. 1 (c)). Subsets of these images were then spatially aligned using the position data of the scan and averaged to improve the SNR. Note that the significant variations of the probe's intensity distribution, which are inherent to structured illumination, manifest as corresponding variations in the SNR over the RPI-reconstructed image. It is therefore beneficial to displace the sample slightly (within the probe size) for averaging RPI reconstructions, which is naturally the case for the ptychographic scan data used in this work, because it results in a more uniform SNR and removes low-SNR gaps in the image. In addition, each image was weighted by the probe's intensity distribution during the averaging in order to reduce the contribution of low-SNR regions. This postprocessing significantly improves the image resolution even when averaging only a few images. These results are presented in Section 5. Our first demonstration of single-frame image reconstruction using a table-top HHG-EUV source by applying the RPI algorithm, along with the corresponding ptychographic image of the sample obtained with the diffuser mask, is shown on the right side of Fig. 1 (a) and in Fig. 3 (b).

3. Impact of illumination on randomized probe imaging

First, the impact of the different illuminating beams on the single-frame RPI reconstruction without image averaging was investigated. To enable a comparative study, the number of incident photons on the sample was maintained at a fixed value of 8×10^4 photons for each illumination

Optics EXPRESS

type by adjusting the exposure time to 0.10 s, 0.16 s, and 0.60 s for the pinhole, spiral, and EUV diffuser masks, respectively, in order to compensate for their different relative transmission efficiencies [59]. The reconstructed probes and objects as well as the objects' resolutions from both the ptychography and RPI methods for the pinhole, spiral, and EUV diffuser masks are shown in Fig. 2 (a)-(c), respectively. The image quality and resolution for each illumination, for both ptychography and RPI, were assessed using Fourier ring correlation (FRC) [65], a measure of correlation between two reconstructed images from independent measurements in Fourier space. Thus, we recorded two identical but statistically independent scans for each illumination condition and performed both reconstruction methods on them. As illustrated in Fig. 2 (a), the pinhole mask produces an unstructured and smooth illumination that is brightest at and around the center of the beam, as evident in the reconstructed probe image. Consequently, only features near the center are visible in the RPI-reconstructed image, while the surrounding regions appear very noisy due to insufficient illumination intensity. To ensure a meaningful FRC analysis for the pinhole and spiral masks, an aperture (indicated by the black circles in Fig. 2 (a) and (b)) was therefore applied to the image, restricting the resolution calculation within the aperture by excluding the noisy surroundings. This yields a spatial half-pitch resolution of 540 nm. The spatial resolution improves to 260 nm when using the spiral mask and even reaches 160 nm with the EUV diffuser mask. On the other hand, the image resolutions obtained from ptychography reconstructions are substantially higher than those from the RPI reconstructions. Interestingly, a half-pitch resolution of 80 nm is achieved even with the pinhole mask, while the spiral and EUV diffuser masks yield resolutions of 68 nm and 61 nm, respectively. As expected, the images reconstructed via ptychography exhibit superior sharpness, minimal background noise, and clearly resolved features across the entire sample. However, line artifacts appear around the elbow and square structures in the image reconstructed using the pinhole mask (Fig. 2 (a)), as commonly seen with smooth, unstructured beams [59,66,67].

We have demonstrated that single-frame RPI reconstructions were successful for all three types of illuminating beams in the EUV region. Nevertheless, the RPI reconstruction is sensitive and highly dependent on the illumination structure since the reconstruction utilizes only a single diffraction pattern. Structured illumination has been shown to enhance the image resolution in ptychography reconstructions by introducing spatial frequency variations in the recorded diffraction patterns [66–68]. In other words, a beam with a structured wavefront induces varying intensity and phase diversity in the diffraction patterns, leading to better convergence and more accurate reconstructions. This improvement arises because the phase retrieval algorithm can more effectively distinguish between the object and the probe. For this reason, the structured illumination produced by the spiral mask yields better image resolution than that of the unstructured illumination from the pinhole, in both ptychography and RPI reconstructions. However, the highest image resolution is achieved with the strongly structured illumination created by the EUV diffuser in both reconstructions. This EUV diffuser, tailored for 13.5 nm based on molybdenum nanostructures [59], creates highly randomized speckle patterns, resulting in widely spread diffraction patterns. Hence, the EUV diffuser mask improves the resolution by about 40% compared to the spiral mask (from 260 nm to 160 nm) in the RPI reconstruction, while the improvement is only about 10% (from 68 nm to 61 nm) in the ptychography reconstruction. This shows that the quality of a single-pattern RPI reconstruction is highly dependent on the spread of the beam's angular spectrum, which not only introduces varying intensity and phase diversity but also determines the sample coverage in a single diffraction pattern due to the beam's divergence after the mask. The divergence significantly increases for the spiral and diffuser masks compared to the pinhole mask. In contrast, ptychography uses a scan of overlapping diffraction patterns covering the entire sample, thus only differences in wavefront diversity affect the reconstruction quality for the same number of photons incident on the sample.

Optics EXPRESS

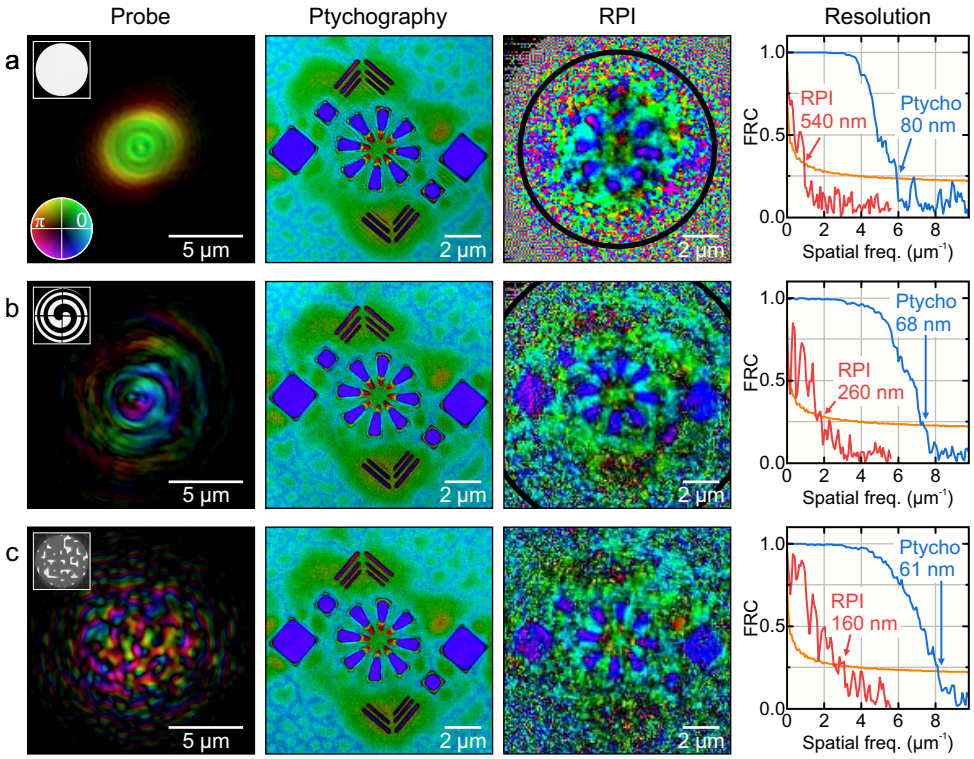

Fig. 2. Comparison of the reconstructed probes and objects using ptychography and RPI algorithms for three different illuminating beams: (a) pinhole, (b) spiral, and (c) EUV diffuser. Color wheel: phase is represented as hue and modulus as brightness. The insets show the corresponding masks. The black circles in (a) and (b) indicate the aperture boundaries where the image transitions into random noise, with the image regions outside the circles excluded from the FRC calculation. Note that the RPI-reconstructed objects are retrieved from a single, selected diffraction pattern. The graphs display the half-pitch resolutions of the reconstructed images, evaluated using FRC with the half-bit criterion (orange lines). All measurements were performed using the same number of photons incident on the sample.

4. Randomized probe imaging at maximum dynamic range

Next, we studied the single-frame RPI reconstruction quality without image averaging using the spiral and EUV diffuser masks at the detector's maximum dynamic range (Fig. 3). As mentioned earlier, an average photon number of approximately 8×10^4 per diffraction pattern was used for all three illuminations. This value corresponds to the exposure level just before the signal captured with the pinhole mask became overexposed, as its exposure time is limited by saturation at the center of the diffraction pattern. Unlike the narrow angular spectrum produced by the pinhole mask, which leads to saturation at the detector center due to its bright, centrally concentrated beam, both the spiral and EUV diffuser masks significantly broaden the angular spectrum of the resulting diffraction patterns. Consequently, the diffraction patterns are more evenly distributed across the detector, thereby relaxing the detector's dynamic range requirements. This allowed us to increase the exposure time for both mask cases to acquire the maximum signal without reaching saturation. Notably, the EUV diffuser mask exhibits an even broader angular spectrum than the spiral mask, as evident from the probe images in Fig. 2 (b) and (c). The former distributes intensity more uniformly across the detector at larger diffraction angles. Specifically, the photons

Optics EXPRESS

are most efficiently spread over the detector due to the diffuser's multiple randomized speckles. As a result, higher photon counts of 3×10^5 and 7×10^5 photons per diffraction pattern were recorded for the spiral and EUV diffuser masks, respectively [59]. The corresponding spatial half-pitch resolutions from the RPI-reconstructed images are estimated to be 120 nm for the spiral mask and 110 nm for the EUV diffuser, respectively. Furthermore, the images reconstructed using the automatic differentiation-based ptychography algorithm employed in this work exhibit resolutions of 52 nm for the spiral mask and 40 nm for the EUV diffuser mask (Fig. 3 (a) and (b)), while slightly better resolutions of 45 nm and 32 nm, respectively, have been achieved [59] using the PtyLab framework [69]. This can be attributed to the absence of the orthogonal probe relaxation algorithm [70] in the current reconstruction method, which is known to enhance reconstruction quality by allowing a set of orthogonal probe modes to adapt dynamically to illumination variations. Overall, the highest image resolution was achieved with the EUV diffuser in both reconstructions when utilizing the detector's full dynamic range.

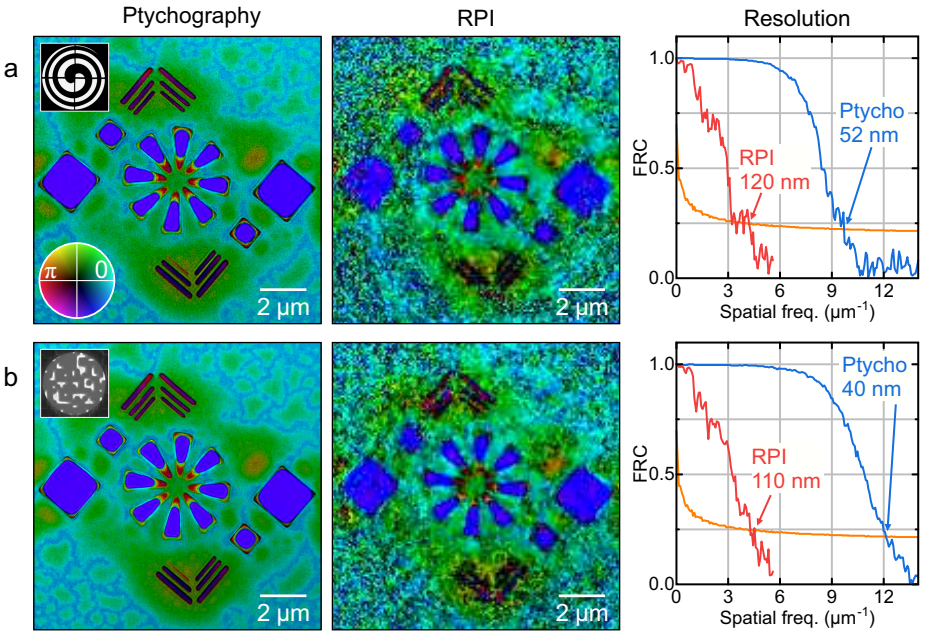

Fig. 3. Comparison of the reconstructed objects using ptychography and RPI algorithms for two different illuminating beams: (a) spiral and (b) EUV diffuser. Color wheel: phase is represented as hue and modulus as brightness. The insets show the corresponding masks. Note that the RPI-reconstructed objects are retrieved from a single, selected diffraction pattern. The graphs display the half-pitch resolutions of the reconstructed images, evaluated using FRC with the half-bit criterion (orange lines). The measurements of both spiral and EUV diffuser cases were performed using the maximum dynamic range of the detector.

5. Averaged randomized probe imaging

The capability of RPI to reconstruct the object from a single diffraction pattern, albeit at a decreased resolution compared to a ptychography scan, offers a granular trade-off between SNR and acquisition time for applications that are limited by measurement duration, such as online feedback or time-resolved pump-probe experiments. Figure 4 shows a substantial increase in SNR and, therefore, improved image resolution when averaging independently RPI-reconstructed images using different subsets of the diffraction patterns from the ptychography scan for the

Optics EXPRESS

pinhole (Fig. 4 (a)), spiral (Fig. 4 (b)), and EUV diffuser (Fig. 4 (c)) masks, respectively. The description of the image averaging process is provided in Section 2. Note that the maximum dynamic range illumination condition was used for the spiral and EUV diffuser masks. Since the EUV beam illuminated different parts of the sample at different scan steps, each reconstructed image was weighted by the spatial distribution of the probe before averaging in order to eliminate noise outside the illumination area from contributing to the average. The image quality improves significantly when averaging about 10 images, and approaches ptychography-like quality (though with slightly reduced feature sharpness) for about 100 averaged images for both the spiral and EUV diffuser masks. The image obtained with the pinhole mask remains notably worse compared to ptychography (Fig. 2 (a)), even after averaging the entire scan, but now reveals the entire object since the averaging weighted by the probe effectively combines different regions of the sample illuminated during the scan. Note that for 10 or fewer averaged images, only the central region of the object is illuminated due to the small probe size after the pinhole mask. Hence, for these images, only the illuminated regions indicated by the black circles in Fig. 4 (a) are considered for the FRC analysis, as shown in Fig. 4 (d)-(f) for the pinhole, spiral, and EUV diffuser masks,

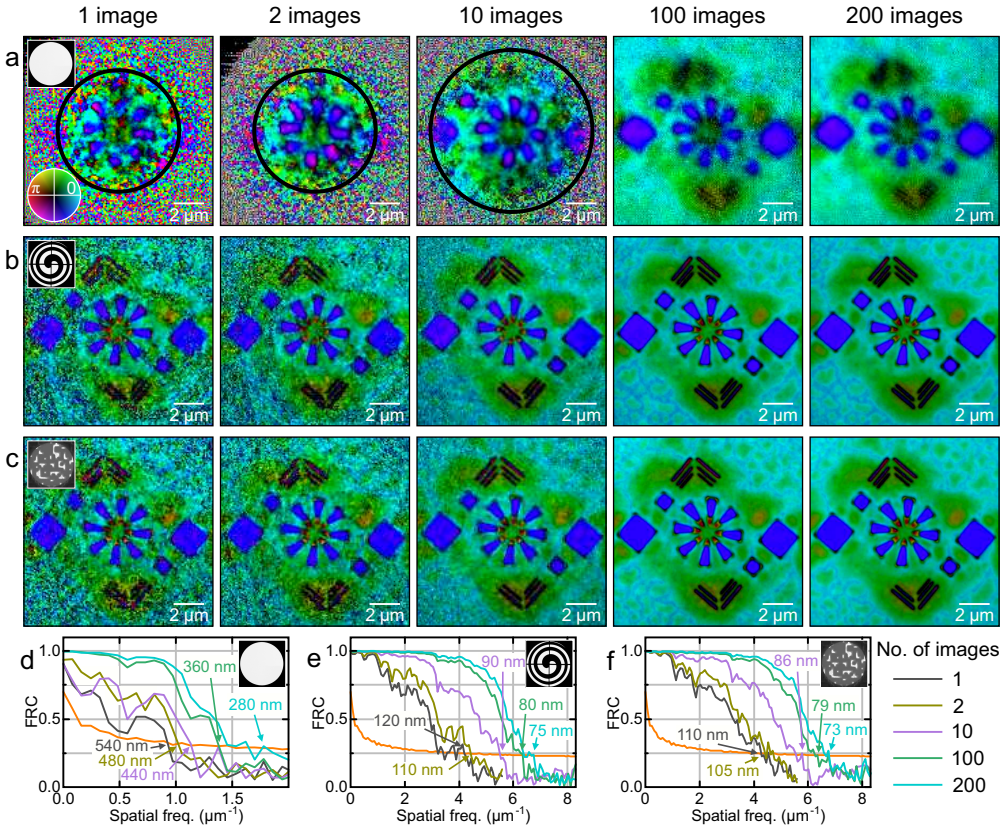

Fig. 4. Comparison of single images and averages of 2, 10, 100 and 200 images, respectively, from the RPI reconstructions for three different illuminating beams: (a) pinhole, (b) spiral, and (c) EUV diffuser. Color wheel: phase is represented as hue and modulus as brightness. Half-pitch resolutions of the corresponding single images and averaged images for the three different beams: (d) pinhole, (e) spiral, and (f) EUV diffuser, evaluated using FRC with the half-bit criterion (orange lines). Note that the measurements of both spiral and EUV diffuser cases were performed using the maximum dynamic range of the detector.

Optics EXPRESS

respectively. The image resolution given by the FRC half-bit criterion improves from 540 nm to 280 nm for the pinhole mask, from 120 nm to 75 nm for the spiral mask, and from 110 nm to 73 nm for the EUV diffuser mask, respectively, when comparing the single-image resolution to 200 averaged images (full scan). For the spiral and EUV diffuser masks, sub-100-nm resolution is achieved for 10 averaged images.

This result demonstrates that overlap between diffraction patterns, which is essential for ptychography, is not necessary to achieve high image resolution with RPI, since each image is independently reconstructed from a single diffraction pattern. The RPI resolution is primarily improved by a large probe coverage of the sample area, as well as signal accumulation (e.g., by averaging multiple images) to increase the SNR. Similar to ptychography, the underlying phase retrieval algorithm used in the RPI technique benefits as well from the wavefront diversity introduced by structured illumination. Hence, the pinhole mask yields the poorest RPI results due to both high uniformity of the probe and low beam coverage of the sample, while the spiral and EUV diffuser masks provide a larger beam coverage due to their broader angular spectrum as well as a high degree of varying intensity and phase diversity, which markedly improves the RPI resolution. Therefore, structured illumination combined with RPI enables high-resolution EUV imaging scans with short image acquisition time or even single-shot imaging [71,72], for example for pump-probe measurements or on-the-fly ptychography. Since such scans are typically performed using the same probe for every scan step, the probe needs to be determined only once via ptychography and can be used for all subsequent RPI reconstructions. If a higher resolution is required than what is achievable with RPI, ptychography reconstructions can be seeded [73] using the RPI results, which can significantly decrease convergence time and allow sparser ptychographic sampling.

6. Discussion and conclusion

In summary, we have demonstrated, for the first time, successful single-frame RPI of an extended sample using a 13.5 nm EUV beam with different illuminations from a table-top HHG source. The RPI algorithm does not require the exact randomized beam used in the original work from Levitan et al. (Reference [54]) but rather it is applicable and well-suited for structured illuminations generated by the spiral-shaped and phase diffuser masks. Our results showed that the structure of the illumination plays a critical role in the quality and resolution of RPI reconstructions. Structured illuminations, particularly those produced by the spiral and EUV diffuser masks, significantly broaden the angular spectrum and spatial frequency content of the recorded diffraction patterns. This not only improves resolution but also enables optimal utilization of the detector's dynamic range. Similarly, structured illumination used in multiwavelength EUV ptychography has been shown to significantly improve reconstruction quality by introducing varying degrees of diversity among different wavelength components and scan positions [74]. It should be noted that the structured beams used in this study were created by placing the tailored masks directly (~200 μm) in front of the sample. However, another promising approach is to drive the HHG process using a structured laser beam itself. This could enable the generation of a broad range of structured beams, including those with orbital angular momentum [75–77], vector beams [78–80], and beam arrays [81,82].

We achieved an image resolution of 110 nm from a single-frame RPI reconstruction using the tailored EUV diffuser and by fully exploiting the detector's dynamic range. In comparison, the image resolution obtained with the spiral mask (120 nm) was only slightly lower, making it a practical alternative due to its common use and ease of fabrication. Nonetheless, we note that the resolution demonstrated here currently lags behind those achieved by FTH [49,83] and CDI [29,84–86]. However, it is important to emphasize that those experiments typically employ high-dynamic-range measurements, in which multiple diffraction patterns with increasing exposure times are combined into a single high-dynamic-range diffraction pattern. Such strategy

Optics EXPRESS

is in principle also compatible with RPI. To achieve higher resolution in single-frame RPI, the use of highly structured beams with diffuse speckle patterns is unequivocally essential to ensure maximal sample coverage and a more even distribution of the diffraction pattern across the detector. Additionally, recent advances in modern high-numerical-aperture EUV meta-optics [87] promise the ability to tailor EUV light fields with reduced speckle, making them highly attractive for high-performance EUV-based RPI.

Furthermore, RPI offers several advantages over other established single-shot lensless imaging modalities, making it particularly promising for future time-resolved pump-probe experiments. These advantages are summarized in Table 1, where RPI is compared with CDI, mask-based FTH and single-shot ptychography [88,89]. The most significant advantage of RPI is its versatility, as it can be readily applied to arbitrary samples without requiring special preparation. For instance, RPI can also be used to investigate samples in reflection geometry, which is not easily achievable with CDI and FTH. In addition, RPI is highly adaptable since it can be implemented in virtually any ptychography setup and does not suffer from low convergence issues which are often encountered in CDI. Single-shot ptychography employing the RPI algorithm together with pre-calibrated illumination for image reconstruction has shown improved resolution compared to the standard algorithm [90]. Moreover, RPI has the advantage over CDI and FTH in directly reconstructing the quantitative object transmission function, rather than the exit surface wave. Even when the probe is pre-characterized in CDI or FTH measurements, reconstruction ambiguities remain, since the relative position of the probe might not be precisely determined.

Table 1. Comparison of RPI with CDI, mask-based FTH, and single-shot ptychography

	RPI	CDI	FTH	Single-shot ptychography
Resolution	Moderate to high	High	High	Moderate
Robustness	High	Low	Very high	High
Sample requirements	None	Isolated	Isolated	None
Measurement in reflection	Yes	Challenging	Challenging	Yes
Quantitative object reconstruction	Yes	No	No	Yes
Implementation in the EUV	Simple	Simple	Simple	Challenging

Overall, the combination of RPI and structured illumination offers a powerful route toward fast, high-resolution single-frame EUV imaging with minimal acquisition time, making it especially suitable for applications limited by acquisition time such as pump-probe experiments of time-resolved dynamics, on-the-fly scans or in situ diagnostics, which can be easily implemented wherever ptychography is performed. Furthermore, it can provide a seed to significantly accelerate ptychography reconstruction of large datasets using the same probe when ultimate resolution is required.

Funding. Freistaat Thüringen (41-5507-2016); Thüringer Aufbaubank (2017 FGR 0076, 2018 FGR 0080, 2023 FGR 0053); Helmholtz Association (Ptychography 4.0, ZT-I-PF-4-018 AsoftXm); Fraunhofer Cluster of Excellence Advanced Photon Sources; HORIZON EUROPE European Research Council (835306, SALT); European Social Fund Plus; Innovation Pool of the Research Field Matter of the Helmholtz Association of German Research Centers (project FISCOV).

Acknowledgement. We thank Abraham L. Levitan for fruitful discussions and for the development and support of the RPI code.

Disclosures. The authors declare no conflicts of interest.

Data availability. Data underlying the results have been used in a previous study [59] and are available at Zenodo in Ref. [59].

Optics EXPRESS

References

1. P. W. Wachulak, A. Bartnik, J. Kostecki, *et al.*, "Extreme ultraviolet and soft X-ray imaging with compact, table top laser plasma EUV and SXR sources," Nucl. Instruments Methods Phys. Res. Sect. B Beam Interact. with Mater. Atoms **364**, 40–48 (2015).
2. B. Rösner, S. Finizio, F. Koch, *et al.*, "Soft x-ray microscopy with 7 nm resolution," Optica **7**(11), 1602–1608 (2020).
3. W. Eschen, R. Klas, D. S. P. Molina, *et al.*, "Coherent nanoscale imaging and chemical mapping with compact extreme ultraviolet and soft x-ray sources: Review and perspective," APL Photonics **10**(5), 50901 (2025).
4. D. Attwood, *Soft X-Rays and Extreme Ultraviolet Radiation: Principles and Applications*, 1st ed. (Cambridge University Press, 2007).
5. L. Loetgering, S. Witte, and J. Rothhardt, "Advances in laboratory-scale ptychography using high harmonic sources [Invited]," Opt. Express **30**(3), 4133–4164 (2022).
6. M. Du, L. Loetgering, K. S. E. Eikema, *et al.*, "Ptychographic optical coherence tomography," Opt. Lett. **46**(6), 1337–1340 (2021).
7. G. Zheng, R. Horstmeyer, and C. Yang, "Wide-field, high-resolution Fourier ptychographic microscopy," Nat. Photonics **7**(9), 739–745 (2013).
8. J. Miao, T. Ishikawa, I. K. Robinson, *et al.*, "Beyond crystallography: Diffractive imaging using coherent x-ray light sources," Science **348**(6234), 530–535 (2015).
9. H. N. Chapman and K. A. Nugent, "Coherent lensless X-ray imaging," Nat. Photonics **4**(12), 833–839 (2010).
10. H. N. Chapman, "Fourth-generation light sources," IUCrJ **10**(3), 246–247 (2023).
11. Y. Chushkin and F. Zontone, "Prospects for coherent X-ray diffraction imaging at fourth-generation synchrotron sources," IUCrJ **12**(3), 280–287 (2025).
12. A. P. Mancuso, O. M. Yefanov, and I. A. Vartanyants, "Coherent diffractive imaging of biological samples at synchrotron and free electron laser facilities," J. Biotechnol. **149**(4), 229–237 (2010).
13. M. J. Bogan, D. Starodub, C. Y. Hampton, *et al.*, "Single-particle coherent diffractive imaging with a soft x-ray free electron laser: towards soot aerosol morphology," J. Phys. B At. Mol. Opt. Phys. **43**(19), 194013 (2010).
14. H. N. Chapman, A. Barty, M. J. Bogan, *et al.*, "Femtosecond diffractive imaging with a soft-X-ray free-electron laser," Nat. Phys. **2**(12), 839–843 (2006).
15. M. Holler, M. Guizar-Sicairos, E. H. R. Tsai, *et al.*, "High-resolution non-destructive three-dimensional imaging of integrated circuits," Nature **543**(7645), 402–406 (2017).
16. T. Li, M. Kahnt, T. L. Sheppard, *et al.*, "X-Ray Multibeam Ptychography at up to 20 keV: Nano-Lithography Enhances X-Ray Nano-Imaging," Adv. Sci. **11**(30), 2310075 (2024).
17. J. Miao, "Computational microscopy with coherent diffractive imaging and ptychography," Nature **637**(8045), 281–295 (2025).
18. Z. Ding, S. Gao, W. Fang, *et al.*, "Three-dimensional electron ptychography of organic–inorganic hybrid nanostructures," Nat. Commun. **13**(1), 4787 (2022).
19. M. Rose, T. Senkbeil, A. R. von Gundlach, *et al.*, "Quantitative ptychographic bio-imaging in the water window," Opt. Express **26**(2), 1237–1254 (2018).
20. R. Górecki, C. C. Polo, T. A. Kalile, *et al.*, "Ptychographic X-ray computed tomography of porous membranes with nanoscale resolution," Commun. Mater **4**(1), 68 (2023).
21. M. Ferray, A. L'Huillier, X. F. Li, *et al.*, "Multiple-harmonic conversion of 1064 nm radiation in rare gases," J. Phys. B At. Mol. Opt. Phys. **21**(3), L31–L35 (1988).
22. Z. Chang, A. Rundquist, H. Wang, *et al.*, "Generation of Coherent Soft X Rays at 2.7 nm Using High Harmonics," Phys. Rev. Lett. **79**(16), 2967–2970 (1997).
23. T. Popmintchev, M.-C. Chen, A. Bahabad, *et al.*, "Phase matching of high harmonic generation in the soft and hard X-ray regions of the spectrum," Proc. Natl. Acad. Sci. **106**(26), 10516–10521 (2009).
24. A. S. Johnson, D. R. Austin, D. A. Wood, *et al.*, "High-flux soft x-ray harmonic generation from ionization-shaped few-cycle laser pulses," Sci. Adv. **4**(5), eaar3761 (2018).
25. J. Gao, J. Wu, Z. Lou, *et al.*, "High-order harmonic generation in an x-ray range from laser-induced multivalent ions of noble gas," Optica **9**(9), 1003–1008 (2022).
26. T. Popmintchev, M.-C. Chen, D. Popmintchev, *et al.*, "Bright Coherent Ultrahigh Harmonics in the keV X-ray Regime from Mid-Infrared Femtosecond Lasers," Science **336**(6086), 1287–1291 (2012).
27. R. Klas, A. Kirsche, M. Gebhardt, *et al.*, "Ultra-short-pulse high-average-power megahertz-repetition-rate coherent extreme-ultraviolet light source," PhotoniX **2**(1), 4 (2021).
28. A. Kirsche, M. Gebhardt, R. Klas, *et al.*, "Continuously tunable high photon flux high harmonic source," Opt. Express **31**(2), 2744–2753 (2023).
29. R. L. Sandberg, A. Paul, D. A. Raymondson, *et al.*, "Lensless Diffractive Imaging Using Tabletop Coherent High-Harmonic Soft-X-Ray Beams," Phys. Rev. Lett. **99**(9), 98103 (2007).
30. S. Witte, V. T. Tenner, D. W. E. Noom, *et al.*, "Lensless diffractive imaging with ultra-broadband table-top sources: from infrared to extreme-ultraviolet wavelengths," Light: Sci. Appl. **3**(3), e163 (2014).
31. M. Hentschel, R. Kienberger, C. Spielmann, *et al.*, "Attosecond metrology," Nature **414**(6863), 509–513 (2001).
32. P. M. Paul, E. S. Toma, P. Breger, *et al.*, "Observation of a Train of Attosecond Pulses from High Harmonic Generation," Science **292**(5522), 1689–1692 (2001).

Optics EXPRESS

33. T. Gaumnitz, A. Jain, Y. Pertot, *et al.*, "Streaking of 43-attosecond soft-X-ray pulses generated by a passively CEP-stable mid-infrared driver," Opt. Express **25**(22), 27506–27518 (2017).
34. R. Kienberger, E. Goulielmakis, M. Uiberacker, *et al.*, "Atomic transient recorder," Nature **427**(6977), 817–821 (2004).
35. E. Goulielmakis, Z.-H. Loh, A. Wirth, *et al.*, "Real-time observation of valence electron motion," Nature **466**(7307), 739–743 (2010).
36. M. Schultze, M. Fieß, N. Karpowicz, *et al.*, "Delay in Photoemission," Science **328**(5986), 1658–1662 (2010).
37. S. Baker, J. S. Robinson, C. A. Haworth, *et al.*, "Probing Proton Dynamics in Molecules on an Attosecond Time Scale," Science **312**(5772), 424–427 (2006).
38. G. Sansone, F. Kelkensberg, J. F. Pérez-Torres, *et al.*, "Electron localization following attosecond molecular photoionization," Nature **465**(7299), 763–766 (2010).
39. L. He, S. Sun, P. Lan, *et al.*, "Filming movies of attosecond charge migration in single molecules with high harmonic spectroscopy," Nat. Commun. **13**(1), 4595 (2022).
40. A. L. Cavalieri, N. Müller, T. Uphues, *et al.*, "Attosecond spectroscopy in condensed matter," Nature **449**(7165), 1029–1032 (2007).
41. S. Neppl, R. Ernstorfer, E. M. Bothschafter, *et al.*, "Attosecond Time-Resolved Photoemission from Core and Valence States of Magnesium," Phys. Rev. Lett. **109**(8), 87401 (2012).
42. M. Schultze, K. Ramasesha, C. D. Pemmaraju, *et al.*, "Attosecond band-gap dynamics in silicon," Science **346**(6215), 1348–1352 (2014).
43. B. Förg, J. Schötz, F. Süßmann, *et al.*, "Attosecond nanoscale near-field sampling," Nat. Commun. **7**(1), 11717 (2016).
44. M. Ossiander, J. Riemensberger, S. Neppl, *et al.*, "Absolute timing of the photoelectric effect," Nature **561**(7723), 374–377 (2018).
45. J. Rothhardt and L. Loetgering, "Ultrafast Nanoscale Imaging with High Harmonic Sources," in *Structural Dynamics with X-Ray and Electron Scattering* (Royal Society of Chemistry, 2023).
46. J. Miao, P. Charalambous, J. Kirz, *et al.*, "Extending the methodology of X-ray crystallography to allow imaging of micrometre-sized non-crystalline specimens," Nature **400**(6742), 342–344 (1999).
47. D. Shapiro, P. Thibault, T. Beetz, *et al.*, "Biological imaging by soft x-ray diffraction microscopy," Proc. Natl. Acad. Sci. **102**(43), 15343–15346 (2005).
48. S. Eisebitt, J. Lüning, W. F. Schlotter, *et al.*, "Lensless imaging of magnetic nanostructures by X-ray spectro-holography," Nature **432**(7019), 885–888 (2004).
49. R. L. Sandberg, D. A. Raymondson, C. La-o-vorakiat, *et al.*, "Tabletop soft-x-ray Fourier transform holography with 50 nm resolution," Opt. Lett. **34**(11), 1618–1620 (2009).
50. D. Gauthier, M. Guizar-Sicairos, X. Ge, *et al.*, "Single-shot Femtosecond X-Ray Holography Using Extended References," Phys. Rev. Lett. **105**(9), 93901 (2010).
51. P. Thibault, M. Dierolf, A. Menzel, *et al.*, "High-Resolution Scanning X-ray Diffraction Microscopy," Science **321**(5887), 379–382 (2008).
52. A. M. Maiden and J. M. Rodenburg, "An improved ptychographical phase retrieval algorithm for diffractive imaging," Ultramicroscopy **109**(10), 1256–1262 (2009).
53. P. Thibault, M. Dierolf, O. Bunk, *et al.*, "Probe retrieval in ptychographic coherent diffractive imaging," Ultramicroscopy **109**(4), 338–343 (2009).
54. A. L. Levitan, K. Keskinbora, U. T. Sanli, *et al.*, "Single-frame far-field diffractive imaging with randomized illumination," Opt. Express **28**(25), 37103–37117 (2020).
55. F. Zhang, B. Chen, G. R. Morrison, *et al.*, "Phase retrieval by coherent modulation imaging," Nat. Commun. **7**(1), 13367 (2016).
56. X. Dong, X. Pan, C. Liu, *et al.*, "Single shot multi-wavelength phase retrieval with coherent modulation imaging," Opt. Lett. **43**(8), 1762–1765 (2018).
57. R. Klas, W. Eschen, A. Kirsche, *et al.*, "Generation of coherent broadband high photon flux continua in the XUV with a sub-two-cycle fiber laser," Opt. Express **28**(5), 6188–6196 (2020).
58. W. Eschen, L. Loetgering, V. Schuster, *et al.*, "Material-specific high-resolution table-top extreme ultraviolet microscopy," Light: Sci. Appl **11**(1), 117 (2022).
59. W. Eschen, C. Liu, M. Steinert, *et al.*, "Structured illumination ptychography and at-wavelength characterization with an EUV diffuser at 13.5 nm wavelength," Opt. Express **32**(3), 3480–3491 (2024).
60. W. Eschen, C. Liu, D. S. Penagos Molina, *et al.*, "High-speed and wide-field nanoscale table-top ptychographic EUV imaging and beam characterization with a sCMOS detector," Opt. Express **31**(9), 14212–14224 (2023).
61. S. Ghosh, Y. S. G. Nashed, O. Cossairt, *et al.*, "ADP: Automatic differentiation ptychography," in *2018 IEEE International Conference on Computational Photography (ICCP)* (2018), pp. 1–10.
62. S. Kandel, S. Maddali, M. Allain, *et al.*, "Using automatic differentiation as a general framework for ptychographic reconstruction," Opt. Express **27**(13), 18653–18672 (2019).
63. P. Thibault and A. Menzel, "Reconstructing state mixtures from diffraction measurements," Nature **494**(7435), 68–71 (2013).
64. D. P. Kingma and J. Ba, "Adam: A Method for Stochastic Optimization," arXiv (2017).

Optics EXPRESS

65. W. O. Saxton and W. Baumeister, "The correlation averaging of a regularly arranged bacterial cell envelope protein," J. Microsc. **127**(2), 127–138 (1982).
66. M. Guizar-Sicairos, M. Holler, A. Diaz, *et al.*, "Role of the illumination spatial-frequency spectrum for ptychography," Phys. Rev. B **86**(10), 100103 (2012).
67. M. Odstrčil, M. Lebugle, M. Guizar-Sicairos, *et al.*, "Towards optimized illumination for high-resolution ptychography," Opt. Express **27**(10), 14981–14997 (2019).
68. A. M. Maiden, G. R. Morrison, B. Kaulich, *et al.*, "Soft X-ray spectromicroscopy using ptychography with randomly phased illumination," Nat. Commun. **4**(1), 1669 (2013).
69. L. Loetgering, M. Du, D. B. Flaes, *et al.*, "PtyLab.m/py/jl: a cross-platform, open-source inverse modeling toolbox for conventional and Fourier ptychography," Opt. Express **31**(9), 13763–13797 (2023).
70. M. Odstrcil, P. Baksh, S. A. Boden, *et al.*, "Ptychographic coherent diffractive imaging with orthogonal probe relaxation," Opt. Express **24**(8), 8360–8369 (2016).
71. A. Ravasio, D. Gauthier, F. R. N. C. Maia, *et al.*, "Single-Shot Diffractive Imaging with a Table-Top Femtosecond Soft X-Ray Laser-Harmonics Source," Phys. Rev. Lett. **103**(2), 28104 (2009).
72. K. Kharitonov, M. Mehrjoo, M. Ruiz-Lopez, *et al.*, "Single-shot ptychography at a soft X-ray free-electron laser," Sci. Rep **12**(1), 14430 (2022).
73. S. Dong, P. Nanda, R. Shiradkar, *et al.*, "High-resolution fluorescence imaging via pattern-illuminated Fourier ptychography," Opt. Express **22**(17), 20856–20870 (2014).
74. A. Pelekanidis, F. Zhang, M. Gouder, *et al.*, "Illumination diversity in multiwavelength extreme ultraviolet ptychography," Photon. Res **12**(12), 2757–2771 (2024).
75. C. Hernández-García, A. Picón, J. San Román, *et al.*, "Attosecond Extreme Ultraviolet Vortices from High-Order Harmonic Generation," Phys. Rev. Lett. **111**(8), 83602 (2013).
76. B. Wang, N. J. Brooks, P. Johnsen, *et al.*, "High-fidelity ptychographic imaging of highly periodic structures enabled by vortex high harmonic beams," Optica **10**(9), 1245–1252 (2023).
77. M. Zürch, C. Kern, P. Hansinger, *et al.*, "Strong-field physics with singular light beams," Nat. Phys. **8**(10), 743–746 (2012).
78. K. G. Miller, J. R. Pierce, F. Li, *et al.*, "Photon acceleration of high-intensity vector vortex beams into the extreme ultraviolet," Commun. Phys. **8**(1), 229 (2025).
79. F. Kong, C. Zhang, H. Larocque, *et al.*, "Vectorizing the spatial structure of high-harmonic radiation from gas," Nat. Commun. **10**(1), 2020 (2019).
80. A. de las Heras, A. K. Pandey, J. S. Román, *et al.*, "Extreme-ultraviolet vector-vortex beams from high harmonic generation," Optica **9**(1), 71–79 (2022).
81. L. Guo, Z. Feng, Y. Fu, *et al.*, "Generation of vector beams array with a single spatial light modulator," Opt. Commun **490**, 126915 (2021).
82. D. D. Schmidt, J. M. Pablos-Marín, C. Clarke, *et al.*, "Self-interfering high harmonic beam arrays driven by Hermite–Gaussian beams," APL Photonics **10**(6), 60801 (2025).
83. G. K. Tadesse, W. Eschen, R. Klas, *et al.*, "High resolution XUV Fourier transform holography on a table top," Sci. Rep. **8**(1), 8677 (2018).
84. M. Zürch, J. Rothhardt, S. Hädrich, *et al.*, "Real-time and Sub-wavelength Ultrafast Coherent Diffraction Imaging in the Extreme Ultraviolet," Sci. Rep. **4**(1), 7356 (2014).
85. G. K. Tadesse, R. Klas, S. Demmler, *et al.*, "High speed and high resolution table-top nanoscale imaging," Opt. Lett. **41**(22), 5170–5173 (2016).
86. M. D. Seaberg, D. E. Adams, E. L. Townsend, *et al.*, "Ultrahigh 22 nm resolution coherent diffractive imaging using a desktop 13 nm high harmonic source," Opt. Express **19**(23), 22470–22479 (2011).
87. M. Ossiander, M. L. Meretska, H. K. Hampel, *et al.*, "Extreme ultraviolet metalens by vacuum guiding," Science **380**(6640), 59–63 (2023).
88. X. Pan, C. Liu, and J. Zhu, "Single shot ptychographical iterative engine based on multi-beam illumination," Appl. Phys. Lett. **103**(17), 171105 (2013).
89. P. Sidorenko and O. Cohen, "Single-shot ptychography," Optica **3**(1), 9–14 (2016).
90. A. Levitan, K. Wakonig, Z. Gao, *et al.*, "Single-shot x-ray ptychography as a structured illumination method," Opt. Lett. **50**(2), 443–446 (2025).